High-Speed Synchronous Reluctance Motor for Electric-Spindle Application

Emanuel Castagnaro, Nicola Bianchi

***Abstract*—In last years, high speed integral motor spindles are obtaining attentions due to their compact frame. The actual choice for raw plastic and wood materials processing are the induction motor and the interior permanent magnet machine. In particular, permanent magnet motors are suitable for wide constant power-speed range; they show high power density and high power factor. However, the increasing cost of rare-earth magnets leads the designer to investigate other solutions. For this sake, this paper deals with the design procedure of a high-speed free rare-earth motor for a electric-spindle applications. Hereafter, the synchronous reluctance machine is investigated. Such a machine represents a valid alternative thanks to the absence of rare-earth magnets and, consequently, the reduced cost. The goal of this study is to show the feasibility of such a high-speed motor. For this aim, a 4.5 kW motor at the maximum rotation speed of 20 000 rpm is designed. A multi-objective optimization process is proved to be an useful tool for this sake. The best individual is capable to deliver the rated power at both base speed and maximum speed. Synchronous reluctance machine proves to be a good free rare-earth candidate for high speed integral motor spindle applications.**

I. Introduction

CONSIDERING the machine tool sector for raw materials processing, both belt-driven and Integral Motor Spindles (IMSs) are solutions widely used. IMSs are considered as a valid choice for High-Speed (HS) applications thanks to the absence of the belt-pulley system. IMSs find applications in rotating-cutter working machines, grinding machines, milling machines and so on. Since IMS usually work at HSs requiring wide constant power-speed range, the induction motors [1] and Interior Permanent Magnet (IPM) machines [2]–[4] are commonly used. In particular, IPM motors show high power density and power factor; they are a suitable solution. However, the increasing cost of rare-earth magnets and the market uncertainties push the industry to find other solutions.

Even if the Synchronous Reluctance (SynRel) motor has been proposed several years ago, only recently it is more and more adopted in various applications due to its robustness, the high efficiency combined with the lack of permanent magnets. SynRel motors are becoming attractive in many fields and applications requiring high dynamic, high torque density and fault-tolerant capability such as traction and household appliances. This is due to the excellent features in terms of: HS capabilities, absence of excitation winding, lack (or low amount) of permanent magnets in the rotor structure [5], [6].

This work has been also supported by means of the department project SID 2018 BIRD 180470.

E. Castagnaro and N. Bianchi are with the Electrical Drives Laboratory, Department of Industrial Engineering, University of Padova, Via Gradenigo 6A, Padova, 35131, Italy.

TABLE I
Problem requirements, constraints and hypotheses.

Requirements			
Rated power	P_n	4.5	kW
Rated mechanical speed	n_n	9000	rpm
Maximum mechanical speed	n_{max}	20 000	rpm
Constraints			
Stator outer diameter	D_e	107	mm
Stator diameter	D	107	mm
Shaft diameter	D_s	18	mm
Stack length	L_{stk}	110	mm
Rated voltage	V_n	380	V
Hypotheses			
Electric loading	$\hat{K}_s$	35	kA/m
Slot current density	J	5	A/mm^2
Slot fill factor	K_{fill}	0.4	
Number of poles	$2p$	4	
Number of slots	Q	24	
Number of slots per pole per phase	q	2	
Air-gap	g	0.4	mm
Iron lamination yield strength	σ_y	450	MPa
Safety factor	s_f	1.5	

A substantial advantage is also the absence of the rotor iron losses [7], which decreases the rotor temperature if compared with IM drives. However, if not properly designed, SynRel machine suffers of some drawbacks, such as high torque ripple and low power factor. For low speed motors the design methodology is well established [8]. Many works have been carried out in the field of torque density and torque ripple [9], [10].

At HS the machine design becomes a hard task. Fig. 1 shows the cross-section area of a rotor pole: SynRel rotors are characterized by flux-barriers and iron-channels; the centrifugal forces can compromise the mechanical integrity of the rotor. Together with the electromagnetic one the mechanical design becomes of fundamental importance to achieve feasibility at HSs while maintaining the optimal performance required.

The goal is to design a HS SynRel motor for IMS. A 4.5 kW motor at the rotational of 20 000 rpm has been designed: a suitable application could be in the sector for the processing of soft raw materials such as wood, plastic and composite. Once the requirements are gave, the project constraints are highlighted and some hypotheses are justified. Then, A multi-objective optimization coupled with a Finite Element (FE) model is carried out in order to find the best design solutions. The best solution performances are subsequently deeply investigated. Moreover, the rotor mechanical feasibility is showed. SynRel

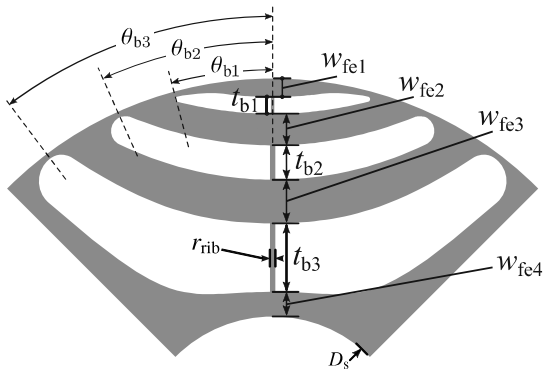

Fig. 1. Sketch of the radial cross-section of the parametrized rotor flux-barriers. The optimization parameters are highlighted.

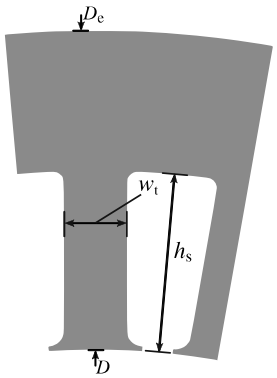

Fig. 2. Sketch of the radial cross-section of the parametrized stator slot. The optimization parameters are highlighted.

machine proves to be a good free rare-earth candidate for HS IMS applications. A prototype has been built to experimentally verified the project feasibility. Unfortunately, at the time the paper has been written it wasn't possible to test it.

II. Preliminary considerations

The specifications are listed in Table I. In the following, these data are briefly commented. These specifications are necessary for its set-up of a multi-objective optimizer.

The motor outer and internal dimensions are the main constraints of the application. In particular, they are 107 mm for the outer diameter D_e, 60 mm for the internal diameter D and 110 mm for the stack length. The shaft diameter D_s is 18 mm: this size is necessary to guarantee enough space for the spindle tip. Also the rated line-to-line voltage is given. It is equal to 380 V.

IMS usually works at HS; the power requirement is 4.5 kW from 9000 rpm up to 20 000 rpm. Considering the machine base point at 9000 rpm, the rated torque is about 5 N m. The dimensions previously reported would lead to a machine active volume equal to 1 dm^3. Assuming now a ratio between the rated torque and the active volume $K_{TV} = 5-6$ N m/dm^3 [11], the constraint size should be sufficient to deliver the desired torque.

To avoid high machine temperatures the electrical loading $\hat{K}_s$ is posed to be around 35 kA/m, $\hat{K}_s$ being computed as:

$$\hat{K}_s = \frac{\sqrt{2} Q J K_{fill} S_{slot}}{\pi D} \tag{1}$$

where Q is the number of stator slots, J is the slot current density, K_{fill} is the slot fill factor and S_{slot} is the slot cross-section area.

The machine pole number is not given but it can be decided by few simple considerations. A low pole number implies lower working frequencies: this would limit both iron and proximity losses. SynRel rotor is characterized by the flux-barrier; a high number of poles could imply rotor manufacturing issues due to the reduced flux-barrier thickness. Moreover, for a given rotor diameter, the higher the pole number the lower the magnetizing inductance. In order to satisfy the latter and not to increase the stator magnetizing current, the pole number is set equal to 4. The choice of the iron lamination also significantly affects the iron losses. Small lamination thickness reduces the eddy-current production. Moreover, at HS, the type of lamination also has a significant impact on the rotor mechanical feasibility. M270-35A lamination is characterized by the highest yield strength among the ferromagnetic materials available. It is equal to 450 N/mm^2.

Since the saliency ratio of concentrated-coil fractional-slot windings is low [12], this causes the decreasing of the machine power factor and the worsening in the torque ripple [13], a distributed integral-slot winding is considered. For an integral-slot winding the number of slot per pole per phase (SPP) q is an integer and higher than 1: due to the low D_e, it is set to be equal to 2 to avoid slot manufacturing issues. As shown in [14], the higher the number of rotor flux-barrier, the lower the torque ripple. Since the previous choice of SPP worsens the stator magneto-motive force harmonic content, a rotor with three flux-barriers per pole has been considered. Finally, the air-gap length g is set equal to 0.4 mm.

III. Choice of the optimal geometry

A. Optimization set-up

The considerations reported in the previous section led to the optimization of $2p = 4$ poles, $q = 2$ SPP geometries. The Differential Evolution (DE) [15] is used as optimization algorithm, which guarantees great performance and convergence in a short time. The parameters of the optimization are 7. They are highlighted in Fig. 1 and Fig. 2. In particular they are: the slot height h_s, the tooth width w_t, the three flux-barrier angles θ_{bi} (with i = 1,2 and 3), the total magnetic insulation ratio k_{air}. According to Fig. 1 it is defined as:

$$k_{air} = \frac{l_{air}}{l_{tot}} \tag{2}$$

where $l_{tot} = (D - D_s - g)/2$ and $l_{air} = t_{b1} + t_{b2} + t_{b3}$ sum of the flux barrier thickness. Therefore k_{air} measures the total quantity of air with respect to the total available length.

The objectives of the optimization are maximization of average torque T_m and minimization of torque ripple ΔT_m. The efficiency η is also been taken into account. It is computed at the Maximum Torque Per Ampere working point (MTPA) at rated current and at the base speed n_n These choices are justified as follows: the first two are classic optimization objectives;

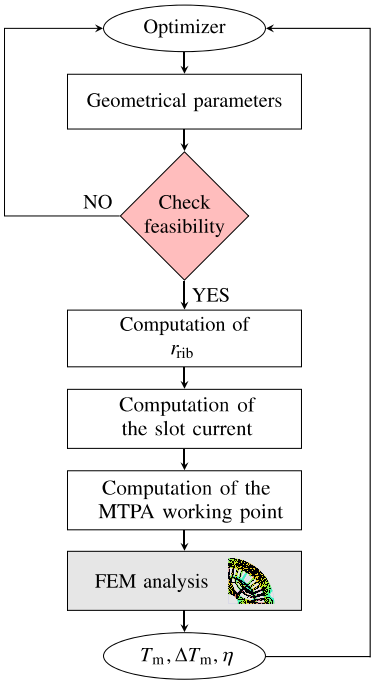

Fig. 3. Flowchart of the optimization procedure used.

in particular, since the IMS power is a project requirement, T_m is a required objective. In Section II, the efficiency has not been mentioned as a requirements. However, since the supply frequency is high (up to 667 Hz at maximum speed), the stator iron losses must be considered. The efficiency is also needed to reach the optimal solution by controlling the stator iron flux densities, neglecting solutions characterized by narrow tooth width and yoke height.

The flowchart of the optimization procedure is showed in Fig. 3: first, the optimizer generates the set of rotor parameters for the individual of the first generation; once the magnetic insulation ratio is decided, the width of each rotor iron path w_{fei} (with i = 1,2,3 and 4) is computed [11] referring to the d-axis flux density distribution.

In HS applications the radial rib r_{rib} sizing is of fundamental importance. The high rotation speeds reached could compromise the mechanical feasibility of the rotor. Since the width of each radial rib strictly depends upon the k_{air} and the flux-barrier angles (*i.e.*, on the rotor iron channels radial position), each r_{rib} thickness is computed based on the optimization parameters. Moreover, their sizing is also based on the maximum speed required and on the assumed safety factor: they are reported in Table I. A semi-analytical method has been implemented within the optimization algorithm [16].

The slot current $I_{s,slot}$ is properly chosen considering a constant current density $J = 5.5\,A/mm^2$ together with the slot area S_{slot}. Once set, the MTPA working point at rated current is found. Finally, the average torque, the torque ripple and the machine efficiency are computed and the cycle restarts.

B. Optimization results

The result of the optimization are reported in Fig. 4 and Fig. 5 showing the objectives planes for all the optimized

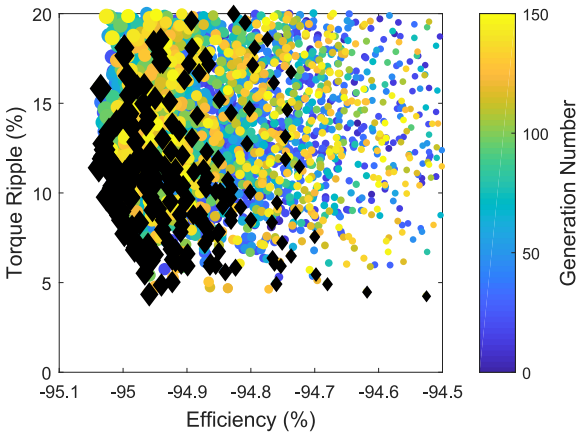

Fig. 4. Efficiency versus torque ripple plane. The markers dimension is proportional to the efficiency.

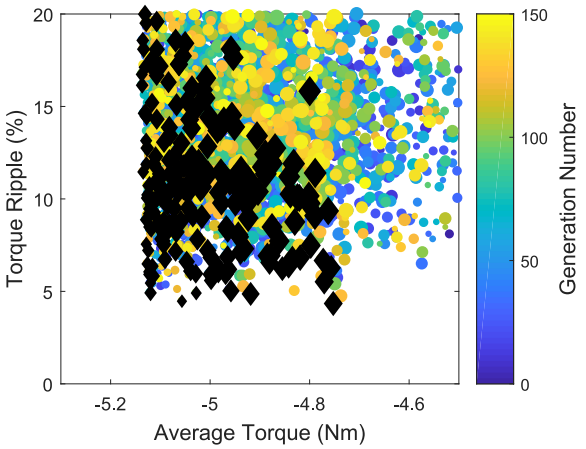

Fig. 5. Efficiency versus average torque plane. The markers dimension is proportional to the efficiency.

individuals. The Pareto solutions are the points closer to the bottom left corner. They are marked with a black diamond. The bright and dark colours denote the generation number. The markers dimension is proportional to the efficiency: the higher the efficiency, the larger the marker dimension.

Considering the $\eta - \Delta T_m$ plane, shown in Fig. 4, the individuals efficiency lies between the 94.5 % up to 95.1 %. They show very different torque ripple ranging from 5% up to 20%.

Considering now the $T_m - \Delta T_m$ plane, the majority of the Pareto solutions satisfying the mechanical torque requirement are marked by small markers and characterized by 'low' efficiency: those optimal individuals are generated by a combination of low t_w and high h_s.

The optimization results are also reported in Fig. 6: where the objectives versus the optimization parameters are shown. As it can be noted, the relations between the average torque and third flux-barrier angles is linear: the wider the flux-barrier, the higher the torque. The same occurs considering the θ_{b3} vs η plot. The slot height and the tooth width also show the same behaviour. In fact, considering the same current density, a higher slot area would imply a greater electrical loading. However, the h_s vs ΔT_m plot shows that machines with a higher

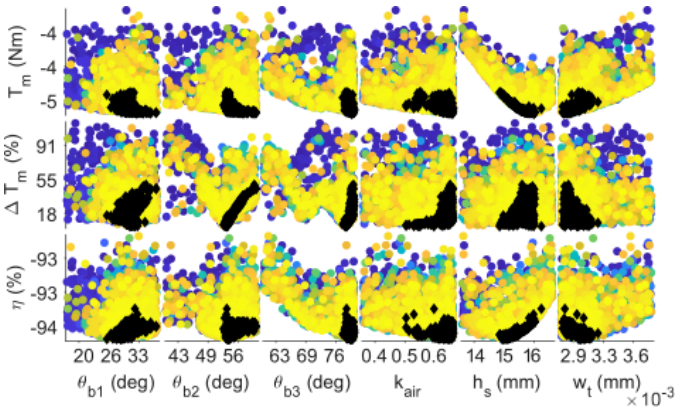

Fig. 6. Overview of the optimization results. Dark colours represent older generations; black diamonds are the Pareto solutions.

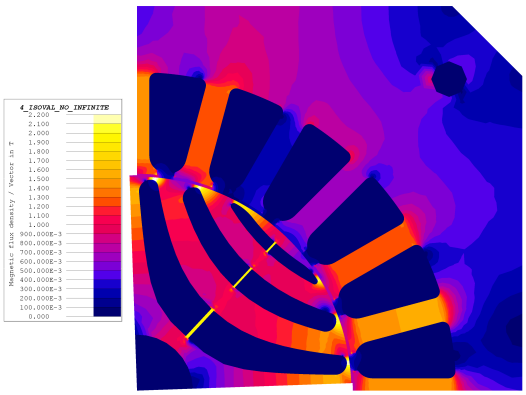

Fig. 7. Radial cross-section of the electromagnetic FE model

slot height display higher torque ripple. The k_{air} vs T_{m} plot also highlights that almost all the Pareto solutions lie near the bottom-right corner: as the generation number increased and due to the high speed of rotation, the optimization algorithm selected lighter rotors characterized by thick flux-barriers. This is to minimize the radial rib thickness.

A final design is chosen among the Pareto solutions. The choice has been made taking into account the rated torque and the trade-off between the torque ripple and the machine efficiency. In particular, the best is capable to deliver the rated power; however, the choice penalizes the other objectives: the torque ripple lies between 7% and 9%. The efficiency is slightly lower than 95%. A more accurate electromagnetic analysis is reported in the next section. The mechanical feasibility of the rotor is also checked.

IV. Final design

A. Electromagnetic analysis

The preliminary FE analyses are carried out on the best design solution found during the optimization process. Its main data are reported in Table II; its magneto-static solution under MTPA working condition is in Fig. 7. The individual chosen among the Pareto solutions in characterized by a wide slot cross-section area. Enough space has been gained increasing the electrical loading. The actual $\hat{K}_{\text{s}}$, that is equal to 36 kA/m,

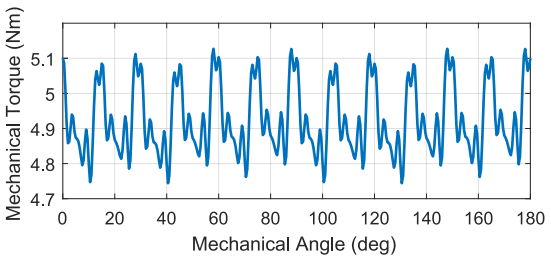

Fig. 8. Torque versus mechanical angle in MTPA working condition.

TABLE II
Machine main data.

Rated Data			
Rated power	P_{n}	4.5	kW
Rated mechanical speed	n_{n}	9000	rpm
Maximum mechanical speed	n_{max}	20 000	rpm
Rated Voltage	V_{n}	380	V
Rated Current	I_{n}	12.8	A
FE results			
Efficiency	η (@ n_{n})	94.9	%
Average Mechanical Torque	T_{m}	4.9	N m
Torque Ripple	ΔT_{m}	8	%

does not satisfy the previous hypothesis. A slightly increase was necessary to reach power the requirement. As it can be seen, the stator iron saturation is not high: the flux density in the stator teeth does not overcome 1.6 T; in the stator joke is at most 1.3 T. The best individual has a square cross-section. Its side is equal to the stator diameter assumed during the optimization phase. This choice, which does not preclude optimization result, was made in order to adapt the prototype on the test bench.

Fig. 8 shows the mechanical torque against the mechanical angle while feeding the machine in the MTPA working point at the rated current. The actual average torque and torque ripple are reported in Table II: they satisfy the optimization predictions.

B. Mapping

To verify the project requirements the power, efficiency and surface loss density maps in the torque versus speed plane have been predicted. The first one allows verifying if the motor is suitable to deliver the rated mechanical power at the highest design speed. The surface loss density map shows the ratio between the total machine losses and the stator outer surface. This quantity is useful since the machine cooling system is designed considering the surface loss density dissipated by the motor at rated power. The motor parameters are computed in the I_{d} - I_{q} plane on an evenly spaced grid of points. For each operating point defined by the current vector $\left(I_{\text{d}}, I_{\text{q}}\right)$, the flux linkages, electromagnetic torque and flux densities are derived. The computation also considers both iron and copper losses. Indeed, the mechanical power (*i.e.*, mechanical torque) is the difference between the electromagnetic power and machine total losses. The outputs computed on the $I_{\text{d}} - I_{\text{q}}$ plane within

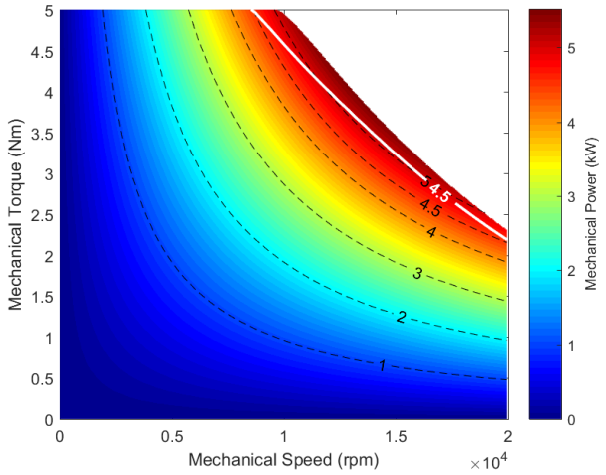

Fig. 9. Mechanical power map in the $T-n$ plane. The output power levels are highlighted in black dashed contour lines. The white solid line represents the surface loss density contour.

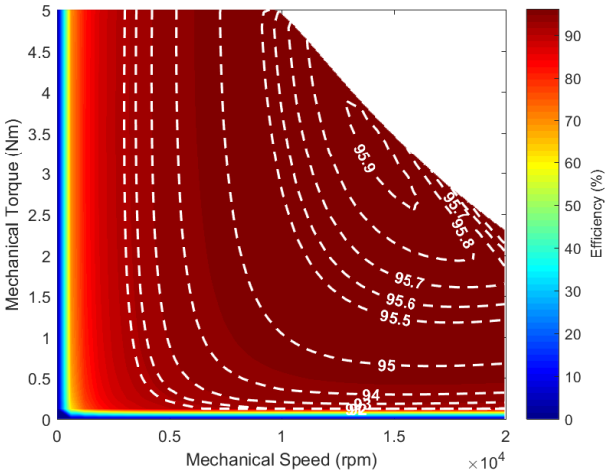

Fig. 10. Efficiency map in the $T-n$ plane. The machine efficiency levels are highlighted by the white dashed contour lines.

current or voltage limits are then plotted in the torque versus speed plane.

The Joule losses computation does consider neither skin nor proximity effects at high frequencies. Indeed, the computation of the winding current distribution would take too much time. Joule losses are computed as:

$$P_{\mathrm{j}} = 3R_{\mathrm{DC}}I^2 \quad R_{\mathrm{DC}} = \frac{Q}{3}n_{\mathrm{c}}\left(L_{\mathrm{stk}} + 2.5\frac{D+h_{\mathrm{s}}}{p}\right)\rho_{\mathrm{Cu,20\,^\circ C}} \tag{3}$$

where $R_{\mathrm{DC}} = 191\,\mathrm{m\Omega}$ is the winding phase resistance, ρ_{Cu} is the wire linear resistance at 20 °C and n_{c} is the number of series conductors per slot. The Joule losses at the rated current are equal to 94 W.

Since the rotor iron losses are negligible if compared with the stator ones, they are not considered. Hence, the stator loss density $p_{\mathrm{s}}(t)$, in W/m^3, is expressed as:

$$p_{\mathrm{s}}(t) = 2k_{\mathrm{hy}}B^2(t)\,f + k_{\mathrm{ec}}\left[\frac{\mathrm{d}B(t)}{\mathrm{d}t}\right]^2 \tag{4}$$

where k_{hy} is the lamination hysteresis coefficient, k_{ec} is the lamination eddy current coefficient and B is the flux density computed in each mesh node and in each time step. The hysteresis coefficient k_{h} is derived from a sinusoidal flux variation over time and is commonly reported in the lamination data sheet. Average losses can be computed, over an electrical period, as:

$$P_{\mathrm{iron}} = \frac{1}{T_{\mathrm{e}}}\int_{T_{\mathrm{e}}}\int_{V_{\mathrm{s}}} p_{\mathrm{s}}(t)\,\mathrm{d}V\mathrm{d}t \tag{5}$$

where T_{e} is the fundamental electrical period and V_{s} is the stator iron volume.

C. Mapping results

The mechanical power map is reported in Fig. 9. The output power levels are highlighted by the black dashed contour lines while the white solid line represents the surface loss density contour at 4.5 kW/m^2. It can be noted that the HS SynRel

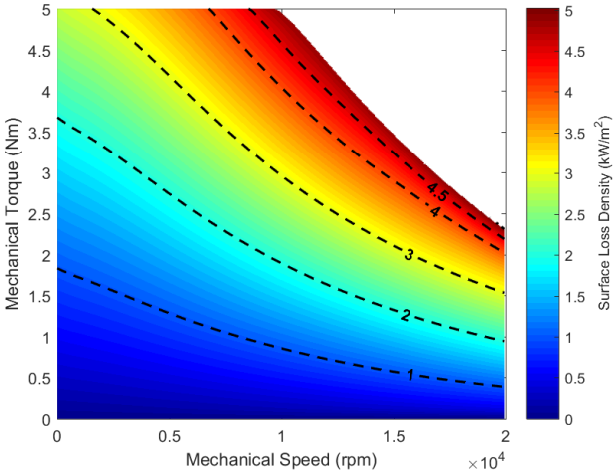

Fig. 11. Surface loss density map in the $T-n$ plane. The surface loss density levels are highlighted by the black dashed contour lines.

motor is able to provide the required rated power from base speed up to the maximum design speed satisfying the project requirements. Indeed, the motor is able to deliver the rated power (4.5 kW) until the maximum speed in flux weakening operation. Moreover, from 10 000 rpm until 18 000 rpm, the available power is up to 5 kW.

Fig. 10 shows the motor efficiency map. The machine efficiency levels are highlighted by the white dashed contour lines. The machine shows a wide high efficiency region (94 % starting from 6000 rpm up to the maximum speed), and it keeps such an efficiency also for lower torque values. This characteristic shows that the motor is suitable for variable-speed duty cycles.

The surface loss density map is reported in Fig. 11. The surface loss density levels are highlighted by the black dashed contour lines. It can be noted that the surface loss density (*i.e.*, the total machine one) increases linearly from the bottom-left part of the $T_{\mathrm{m}}-n$ plane up to its top-right limit. The maximum

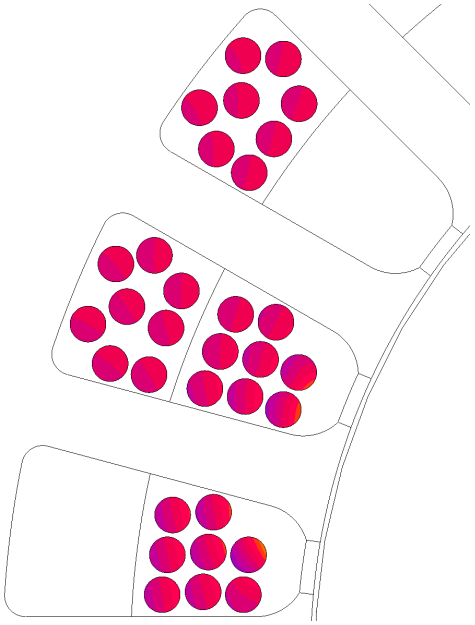

(a)

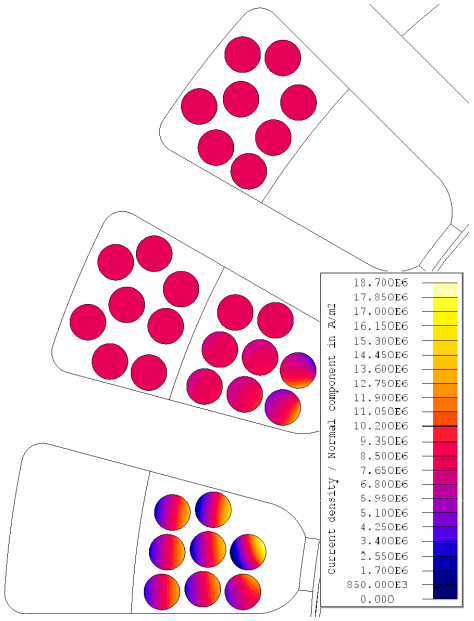

(b)

Fig. 12. Phase peak current density distribution with $n_c = 16$ at (a) 300 Hz (b) 667 Hz. The time instant selected is when the phase current reaches its peak value.

surface loss density that the cooling system has to dissipate lies between 4.5 and 5 kW/m^2. Typical values are 3 kW/m^2 for natural air cooled system and 10 kW/m^2 for forced air ventilation. Considering now Fig. 9, the rated power trajectory in black (4.5 kW) lies below the surface loss density contour in white for each couple (T_m, n). The previous consideration suggests that, in order to let the motor working in continuous duty S1 at rated power, the cooling system power has to be 4.5 kW/m^2.

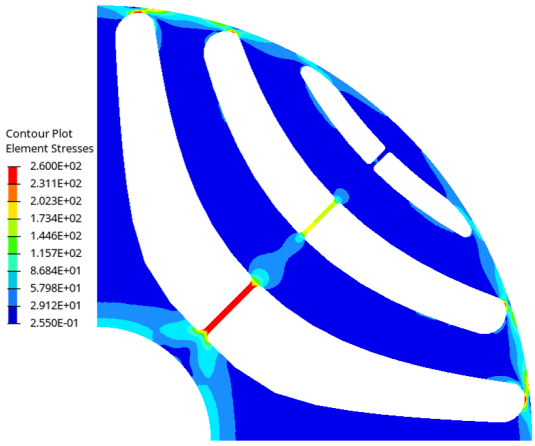

Fig. 13. Radial cross-section of the structural FE model. Units are in MPa.

D. Skin and proximity analysis

In the mapping procedure the Joule losses computation does consider neither skin nor proximity effects: at high operating frequencies they induce an unevenly current distribution within the conductors increasing their resistance. The Joule losses are computed considering the current distribution within the conductors: indeed, copper losses are computed through a transient FE analysis carried out on the whole three-phase winding system. Each slot is filled by n_c series conductors. Each conductor is modelled as a solid one. Simulations are carried out at 9000 and 20 000 rpm and the resulted losses are compared.

Fig. 12(a) and Fig. 12(b) show the phase current distributions. The time instant selected is when the phase current reaches its peak value. It can be noted that the peak current densities are up to 11 A/mm^2 and 18.7 A/mm^2 in some conductors, at 300 and 667 Hz respectively. As reported in Section III, the design peak current density is equal to $\hat{J} = 7.8$ A/mm^2. Hence, the ratio between the computed and the design peak current densities are 1.4 at 9000 and 2.4 at 20 000 rpm, respectively. It means that in some conductors the current density is more than double the DC case.

The simulation which have been performed allows also to compute the Joule losses. They are $P_{j,9000\,rpm} = 96$ W and $P_{j,20\,000\,rpm} = 102$ W. Finally, the AC to DC resistance ratio is computed as the ratio between Joule losses in AC and DC cases. They results as 1.02 and 1.09. As a result, the Joule losses can increase up to the 9% with respect to the DC case in the whole $T_m - n$ plane.

E. Rotor mechanical feasibility

A structural FE analysis is performed to verify that the radial ribs have been properly designed to support the centrifugal load at the maximum rotation speed.

Unlike the electromagnetic FE model, the flux-barrier edges have been rounded since in actual applications sharp edges are not feasible. Moreover, this choice avoids corner dangerous stress concentrations.

The von Mises stress plot is shown in Fig. 13. It can be noted that according to the preliminary considerations, the

Fig. 14. Stator and rotor assemblies.

stresses are lower than the M270-35A yield strength. The maximum stress is located in the third (internal) radial rib; this is an expected result since the internal rib must sustain al the iron channels. In particular the actual safety factor, equal to $s_f = 450/260 = 1.7$, is higher than that assumed in the analytical design. The implemented method leads to a radial ribs over-sizing. However, the higher the safety factor the higher the rotor statical and fatigue resistance [17].

V. Conclusion

The design process of a high-speed small power synchronous reluctance motor for integral motor spindles has been presented. The requests, the hypotheses and the constraints have been the guidelines for this aim. The multi-objective optimization coupled to finite element analysis have proven to be fundamental tools in the design process, in particular when the parameters are many and the objectives may be in contrast with each other. Indeed, the optimization results highlight that the average torque and the machine efficiency are in contrast: machines delivering higher power have low efficiency. The optimization results also showed that the assumptions made have been fulfilled and the requirements have been met.

A final design has been chosen among the optimization results. The choice has been carried out taking into account the rated torque and the trade-off between the torque ripple and the machine efficiency. The overall machine performances have been derived and discussed. The motor is able to exhibit the desired performance. The rotor mechanical feasibility has also been checked. In conclusion, synchronous reluctance machine proved to be a good free rare-earth candidate for small power integral motor spindles.

A prototype, whose stator and rotor stacks are shown in Fig. 14, has been built to confirm the FE prediction by the experimental tests. Unfortunately, at the time the paper has been written it wasn't possible to test it.

References

[1] D. Hong, J. Choi, D. Kim, Y. Chun, B. Woo, and D. Koo, "Development of a high speed induction motor for spindle systems," *IEEE Transactions on Magnetics*, vol. 49, no. 7, pp. 4088–4091, July 2013.

[2] C. Li and B. Kou, "Research on a permanent magnet synchronous motor with parted permanent magnet used for spindle," in *2012 16th International Symposium on Electromagnetic Launch Technology*, May 2012, pp. 1–4.

[3] C. Qin, R. Qu, and D. Li, "Optimal design of v-shaped interior pm synchronous machine with narrow rotor space for electric spindle," in *2016 19th International Conference on Electrical Machines and Systems (ICEMS)*, Nov 2016, pp. 1–5.

[4] J. Rao, L. Zhang, and G. Zhou, "Rotor design and optimizations for interior permanent magnet machines in motorized spindle application," in *2017 20th International Conference on Electrical Machines and Systems (ICEMS)*, Aug 2017, pp. 1–5.

[5] N. Bianchi, S. Bolognani, and B. J. Chalmers, "Salient-rotor PM synchronous motors for an extended flux-weakening operation range," *IEEE Transactions on Industry Applications*, vol. 36, no. 4, pp. 1118–1125, Jul 2000.

[6] A. Vagati, B. Boazzo, P. Guglielmi, and G. Pellegrino, "Ferrite assisted synchronous reluctance machines: A general approach," in *Proceedings of XXth International Conference on Electrical Machines*, Sept 2012, pp. 1315–1321.

[7] E. Castagnaro, G. Bacco, and N. Bianchi, "Impact of geometry on the rotor iron losses in synchronous reluctance motors," *IEEE Transactions on Industry Applications*, vol. 55, no. 6, pp. 5865–5872, Nov 2019.

[8] J. Park, S. Park, M. Lee, J. Chun, and J. Lee, "Rotor design on torque ripple reduction for a synchronous reluctance motor with concentrated winding using response surface methodology," in *INTERMAG 2006 - IEEE International Magnetics Conference*, May 2006, pp. 984–984.

[9] M. Sanada, K. Hiramoto, S. Morimoto, and Y. Takeda, "Torque ripple improvement for synchronous reluctance motor using an asymmetric flux barrier arrangement," *IEEE Transactions on Industry Applications*, vol. 40, no. 4, pp. 1076–1082, July 2004.

[10] S. Taghavi and P. Pillay, "A sizing methodology of the synchronous reluctance motor for traction applications," *IEEE Journal of Emerging and Selected Topics in Power Electronics*, vol. 2, no. 2, pp. 329–340, June 2014.

[11] N. Bianchi, H. Mahmoud, and S. Bolognani, "Fast synthesis of permanent magnet assisted synchronous reluctance motors," *IET Electric Power Applications*, vol. 10, no. 5, pp. 312–318, 2016.

[12] L. Yue, P. Yulong, Y. Yanjun, S. Yanwen, and C. Feng, "Increasing the saliency ratio of fractional slot concentrated winding interior permanent magnet synchronous motors," *IET Electric Power Applications*, vol. 9, no. 7, pp. 439–448, 2015.

[13] C. M. Spargo, B. C. Mecrow, and J. D. Widmer, "Application of fractional slot concentrated windings to synchronous reluctance machines," in *2013 International Electric Machines Drives Conference*, May 2013, pp. 618–625.

[14] G. Bacco and N. Bianchi, "Design criteria of flux-barriers in synchronous reluctance machines," *IEEE Transactions on Industry Applications*, vol. 55, no. 3, pp. 2490–2498, May 2019.

[15] C. Babetto, G. Bacco, and N. Bianchi, "Synchronous reluctance machine optimization for high speed applications," *IEEE Transactions on Energy Conversion*, vol. PP, no. 99, pp. 1–1, 2018.

[16] C. Babetto, G. Bacco, and N. Bianchi, "Design methodology for high-speed synchronous reluctance machines," *IET Electric Power Applications*, vol. 12, no. 8, pp. 1110–1116, 2018.

[17] M. Barcaro, G. Meneghetti, and N. Bianchi, "Structural analysis of the interior pm rotor considering both static and fatigue loading," *IEEE Transactions on Industry Applications*, vol. 50, no. 1, pp. 253–260, Jan 2014.

Biographies

Emanuel Castagnaro received the BS in Industrial Engineering in 2015 and the MS in Electrical Engineering in 2017 from the University of Pavia, Pavia, Italy. Currently he is a PhD student of the Department of Industrial Engineering at the University of Padova. His research interests are mainly focused in the design of Synchronous Reluctance motors and Permanent Magnet motors.

Nicola Bianchi (M'98 SM'09 FM'14) received the M.Sc. and Ph.D. degrees in electrical engineering from the University of Padova, Padova, Italy, in 1991 and 1995, respectively. In 1998, he joined the Department of Electrical Engineering, University of Padova. Since 2018 he has been a Full Professor of electrical machines, converters, and drives in the Electric Drive Laboratory, Department of Electrical Engineering. He is the author or coauthor of several scientific papers and international books on electrical machines and drives. His research interest include the field of design of electrical machines, particularly for drive applications, in which he is responsible for various projects for industries. He has received five awards for best conference and journal papers. He is a member of the Electric Machines Committee and the Electrical Drives Committee of the IEEE Industry Applications Society. He served as a Technical Program Chair for the IEEE Energy Conversion Congress and Exposition 2014 and Associate Editor of the IEEE Transactions on Industry Applications.